Journal of Power Sources 634 (2025) 236505

Contents lists available at ScienceDirect

Journal of Power Sources

journal homepage: www.elsevier.com/locate/jpowsour

Carboxyl-induced microcrystalline regulation of petroleum coke-based carbon anode materials for enhanced sodium storage

Jia-He Lv, Bin He, Lin-Tao Lv, Ming-Kang Yan, Jun-Chen Zhong, Guang-Ping Hao, Wen-Cui Li *

State Key Laboratory of Fine Chemicals, School of Chemical Engineering, Dalian University of Technology, Dalian, 116024, PR China

HIGHLIGHTS

- Chemical group grafting method regulates the graphitization of petroleum coke (PC).
- PC-derived carbon shows extended interlayer spacing and abundant closed pores.
- PC-derived carbon exhibits outstanding sodium storage performance.
- The voltage ranges for the adsorption/insertion-filling mechanism are delineated.

GRAPHICAL ABSTRACT

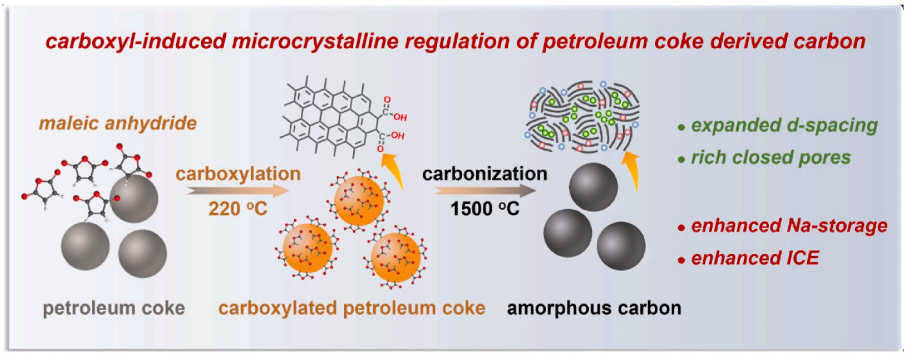

ARTICLE INFO

Keywords:
Petroleum coke
Carbon anode
Sodium-ion batteries
Maleic anhydride
Soft-hard carbon transformation

ABSTRACT

Developing high-performance and low-cost carbon anode materials is crucial for the industrialization of sodium-ion batteries (SIBs) and remains a serious challenge. Petroleum coke (PC) with electrically conductive genes and cost-effectiveness is a promising precursor for the preparation of electrode materials in energy storage. However, as carbon anode precursor for SIBs, its narrow interlayer spacing and ordered graphitic structure limit sodium storage capacity and initial coulombic efficiency (ICE). Herein, a novel carboxyl-induced crosslinking strategy is developed to regulate microcrystalline structure of PC with the aim of enhancing sodium storage while inheriting PC's superior electrical conductivity. A modified Diels-Alder reaction triggered by maleic anhydride over the graphitic edges of ball-milled PC grafts abundant carboxyl groups, which further convert into C-O-C groups during subsequent pyrolysis. Such C-O-C groups sterically restrain the rearrangement of adjacent microcrystalline fragments, resulting in a relatively disordered structure with large interlayer spacing and abundant closed pores. Therefore, remarkable increases in reversible capacity from 106.0 to 326.3 mAh g^{-1} and ICE from 62.3 to 90.0 % are observed. The full cell exhibits an energy density of 228.1 Wh kg^{-1} with excellent cycle stability and rate performance. This carboxyl-induced strategy makes PC possible to be used as anode materials of SIBs.

* Corresponding author.
E-mail address: wencuili@dlut.edu.cn (W.-C. Li).

https://doi.org/10.1016/j.jpowsour.2025.236505
Received 26 November 2024; Received in revised form 15 January 2025; Accepted 10 February 2025
Available online 14 February 2025

1. Introduction

Sodium-ion batteries (SIBs) are emerging as a cost-effective and sustainable alternative to lithium-ion batteries (LIBs) for large-scale energy storage and low-speed electric vehicles due to sodium's abundant and low-cost resources, its high safety, and a similar working principle to LIBs [1–4]. The successful commercialization of LIBs has also enabled the development of electrolytes and cathode materials for SIBs, while the anode materials for SIBs cannot directly borrow from the graphite anodes due to the larger ionic radius of Na^+ (1.02 Å) compared to Li^+ (0.76 Å) [5–7]. Consequently, the development of high-performance and low-cost anode materials is crucial for the commercial application of SIBs.

Carbon-based materials are regarded as the most promising anode candidates for practical SIBs due to their high stability, excellent electrical conductivity and cost-effectiveness [8,9]. Specifically, hard carbon, characterized by short-range microcrystals, large interlayer spacing and abundant closed nanopores, can provide sufficient active sites for sodium ions, which has received extensive attention [10]. Over the past few years, significant efforts and a variety of modification methods have been developed to further enhance the sodium storage properties of hard carbon, such as elemental doping [11–15], activation [16,17] and component optimization [18,19]. Hard carbon is typically derived from the high-temperature pyrolysis of thermoset precursors, such as biomass [20], thermoset resins [21], and organic macromolecules [22]. However, these precursors with low carbon content will release significant volatiles during pyrolysis, resulting in derived carbon material with large specific surface areas [23,24]. The abundance of micropores and defects of the derived carbon induce the formation of a thick solid electrolyte interface (SEI) layer, leading to a low initial coulombic efficiency (ICE) [25,26]. Additionally, the low carbon yield of these precursors significantly diminishes the cost advantage of SIBs [10,27,28]. Therefore, investigating low-cost precursors and achieving high sodium storage capacity along with high ICE are the keys to the commercialization of carbon anodes for SIBs.

Petroleum coke (PC), known for its high carbon yield, cost-effectiveness and electrically conductive genes, is widely recognized as a promising precursor for carbon-based electrode materials in large-scale energy storage applications, such as graphite for LIBs and super activated carbon for supercapacitors. However, as carbon anode precursors for SIBs, the graphitic microcrystalline fragments in PC tend to form highly graphitized soft carbon with narrow interlayer spacing during pyrolysis, leading to unsatisfactory sodium storage performance [29]. For example, R. Alcántara et al. pyrolyzed PC at temperatures below 1000 °C to prepare carbon-based anode materials for SIBs, which only exhibited a reversible specific capacity of about 100 mAh g^{-1} [30]. Thus, while inheriting the excellent conductivity of PC, increasing the sodium storage sites by inhibiting the orderly growth of microcrystalline structure and retarding graphitization is key to achieving high-performance sodium storage in PC-based derived carbon.

Ball-milling has been demonstrated as an effective method for regulating carbon microcrystalline by destroying C-C bonds and distorting the carbon layers [31–33]. For example, Sun Fei et al. effectively regulated the multiscale structure of anthracite-derived carbon through ball-milling treatment, leading to the resulting carbon with amorphous crystallinity and a high content of carboxyl group [31]. The amorphous carbon anode exhibited significantly enhanced sodium storage performance with a reversible specific capacity of 383 mAh g^{-1} at 30 mA g^{-1}. However, ball-milling as a post-treatment process increased the specific surface area of the material, leading to a lower ICE (47.7 %). Furthermore, increasing the crosslinking degree of the precursor is an effective strategy for regulating the microstructure by interfering with the pyrolysis behavior, thereby achieving simultaneous increase in sodium storage capacity and ICE [34,35]. On one hand, increasing the crosslinking degree impedes the orderly stacking of graphitic microcrystalline and promotes the transformation of the microstructure from soft carbon to hard carbon with abundant sodium storage sites, thereby increasing the sodium storage capacity. On the other hand, the crosslinking structure inhibits the significant release of volatiles during the pyrolysis process and reduces the specific surface area and defects, thereby enhancing the ICE. The inert surface of PC poses a significant challenge for achieving direct chemical crosslinking reactions with conventional organic crosslinking agents. Therefore, it is crucial to find a crosslinking method that can effectively graft the crosslinking agent onto the PC to improve the crosslinking degree and achieve microcrystalline structure regulation of PC.

Herein, a carboxyl-induced microcrystalline structure regulation strategy is proposed to transform the microstructure of PC-derived carbon from graphite nanodomains-dominated soft carbon to turbostratic structure-dominated hard carbon. The Diels-Alder reaction between maleic anhydride (MA) and the graphitic edges of ball-milled PC selectively graft carboxyl groups onto the surface of PC. The carboxyl groups are converted into C-O-C groups and facilitate the oxidation-crosslinking of the precursor structure during pyrolysis. Such C-O-C groups act as steric hindrances to inhibit the rearrangement of microcrystalline fragments, retarding graphitization and leading to the formation of disordered structures with enlarged interlayer spacing and abundant closed pores. As a result, the optimized sample (MPCC-1) exhibits enhanced electrochemical performance, with reversible capacity increasing from 106.0 to 326.3 mAh g^{-1} and ICE from 62.3 to 90.0 %, compared to unmodified PC-derived soft carbon. Furthermore, the full cell based on MPCC-1 as the anode and O3-$Na_{0.9}TMO_2$ as the cathode exhibits a high energy density of 228.1 Wh kg^{-1}, demonstrating the great potential of MPCC-1 as a commercial SIBs anode.

2. Experimental section

Material Synthesis: The samples obtained by high-energy ball milling of petroleum coke raw materials (PC, Qingdao, Shandong Province) at 800 rpm were named PC-*x* (*x* represents ball milling time, $x = 0, 1, 2$ h). Maleic anhydride (MA) and PC-*x* were mixed in a mortar at a mass ratio of 2:1. Then, the mixture was heated to 220 °C in a sealed reactor and kept for 8 h to obtain MPC-*x*. To remove unreacted MA, MPC-*x* was washed three times with tetrahydrofuran and dried in a vacuum oven at 50 °C. After that, MPC-*x* was pyrolyzed at 1500 °C for 2 h in an argon atmosphere at a heating rate of 3 °C min^{-1} to obtain MPCC-*x*. Additionally, the petroleum coke raw materials were directly pyrolyzed under the same conditions as MPCC-*x* to obtain PCC as a control sample.

Materials characterization, electrochemical measurement, and correlated calculations: The characterization of material structure and morphology, as well as electrochemical measurements, were provided in the experimental section of the Supplementary Material.

In-situ XRD analysis: The working electrodes were prepared by coating the slurry onto a beryllium window. In-situ cells used the same separator, electrolyte, and sodium sheet as the CR2032 coin-type cells. The E-t curve of the relationship between electrode potential and time during charge and discharge was measured by chronopotentiometry using a CHI 660E electrochemical workstation. The voltage range was set from 0.01 to 3 V, with a current density of 25 mA g^{-1}. Simultaneously, the XRD patterns during charge and discharge were recorded using PANalytical X 'Pert 3 equipment, scanned in steps of 0.02° in the range of 10°–45°.

3. Results and discussion

3.1. Fabrication of petroleum coke-derived carbon and structural characterization

Petroleum coke (PC) is selected as a carbon precursor due to its high carbon content and low ash content (Table S1), which ensures high electrical conductivity, cost-effectiveness and stable electrochemical performance. The preparation process of PC-derived carbon is depicted

in Fig. 1, illustrating the evolution of the material's microstructure. Direct pyrolysis of PC at high-temperature yields a carbon (PCC) with high graphitization and regularly arranged carbon layers, which is due to the growth and rearrangement of microcrystalline fragments in PC. The MPCC-*x* samples are prepared using a two-step pretreatment process. Firstly, PC-*x* (where *x* represents the ball-milling time) is obtained by ball-milling treatment, which disrupts the microcrystalline structure and C-C bonds of PC, resulting in a material with low crystallinity and abundant active graphitic edges. Then, carboxyl groups are grafted via a Diels-Alder reaction between active graphitic edges and maleic anhydride to obtain MPC-*x*. The carboxyl groups convert into C-O-C groups during subsequent pyrolysis, acting as a steric hindrance to prevent the rearrangement of adjacent fragments and retard graphitization. This ultimately leads to the formation of a turbostratic-dominated structure, which is named MPCC-*x*. Additionally, PC is directly reacted with MA to obtain MPC, which is then pyrolyzed into MPCC.

The surface carboxylation of PC was demonstrated by surface functional group analysis and thermogravimetric analysis (TG). A distinct difference between MPCs (MPC and MPC-*x*) and PC samples is observed in the Fourier transform infrared spectroscopy (FTIR) (Fig. 2a). The additional peaks observed at 1850 cm^{-1}, 1710 cm^{-1}, 1390 cm^{-1} and 1190 cm^{-1} in the MPCs samples correspond to the asymmetric C=O stretching mode of the anhydride, C=O stretching mode of the carboxylic acid, C-O-H (O-H bending), and C-OH mode of the carboxylic acid, respectively [36–38]. These peaks confirm that the Diels-Alder reaction has successfully grafted carboxyl groups onto PC. Additionally, the higher spectral intensity in the MPC-*x* samples indicates that the active graphitic edges introduced by ball-milling are beneficial for the grafting of carboxyl groups. The high-resolution C 1s spectra (Fig. 2b) of PC-1 and MPC-1 can be deconvoluted into sp^2 graphitic carbon (284.5 eV), sp^3 hybridized carbon (285.4 eV), C-O (286.3 eV), C=O (287.3 eV), O=C-O (288.5 eV), and the π-π* transition (290–294 eV) [31]. The high-resolution O 1s spectra (Fig. 2c) can be deconvoluted into C-O (531.1 eV), O=C-O (532.4 eV), and C=O (533.8 eV) [39,40]. The fitting results are summarized in Tables S2 and S3. Compared with PC-1, the proportions of sp^3 hybridized carbon and O=C-O in MPC-1 are significantly enhanced, indicating that the Diels-Alder reaction increases the surface defect content and generates abundant carboxyl groups in MPC-1. This is consistent with the FTIR results.

The pyrolysis behavior of the precursors was analyzed by TG-DTG (Fig. 2d and Fig. S1). Based on the DTG data, the weight loss of the precursor can be divided into three distinct stages: 25–300 °C, 300–800 °C and 800–1000 °C. The weight loss in stage I is primarily attributed to the evaporation of moisture and the release of small molecule gas [41]. At stage II, the sample experiences the most significant weight loss. This stage is characterized by extensive dehydrogenation of the hydrogen-rich matrix and the cleavage-reconstruction or self-crosslinking of carboxyl groups, leading to the release of CH_4, H_2 and H_2O [42]. The mass loss in stage III is associated with the decomposition of more stable compounds such as thiophenes, sulfoxides and oxygen-containing heterocycles [43]. The carbon yield of MPC-1 (42.0 %) is higher than that of PC-1 (35.8 %) and the fitted line based on a mixture of PC-1 and MA in equal mass (17.0 %), indicating the formation of a crosslinking structure inhibits the release of volatiles during pyrolysis. Additionally, the maximum weight loss temperature of MPC-1 (382 °C) is higher than that of PC-1 (198 °C), indicating the high thermal stability of the crosslinking structure of MPC-1.

The morphology and microstructure of the samples were

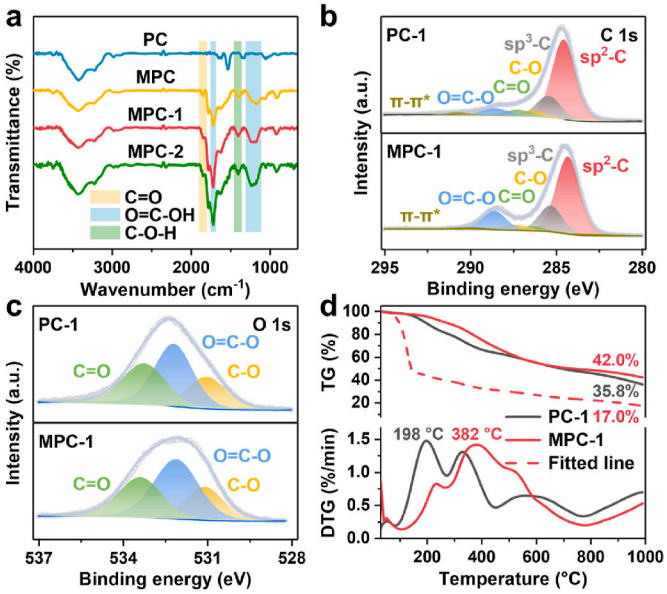

Fig. 2. (a) FTIR spectra of PC, MPC, MPC-1 and MPC-2. High-resolution (b) C 1s, (c) O 1s spectra of PC-1 and MPC-1. (d) TG-DTG curves of PC-1 and MPC-1.

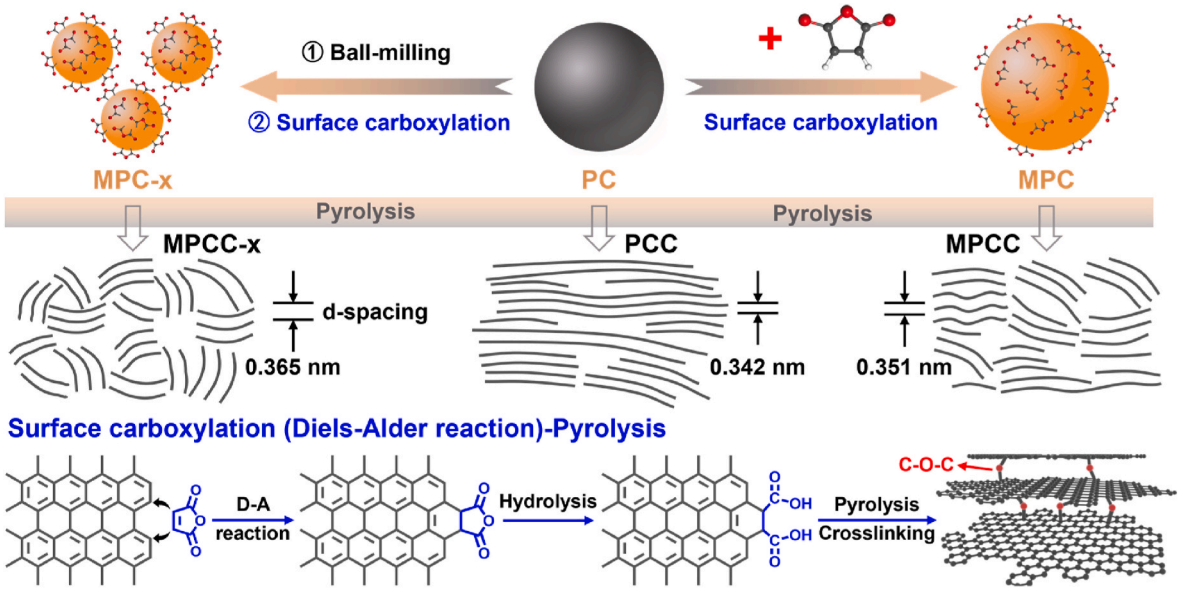

Fig. 1. Schematic illustration of the preparation process of petroleum coke-derived carbon.

characterized by scanning electron microscopy (SEM) and high-resolution transmission electron microscopy (HRTEM). The SEM results (Fig. S2) show that, unlike PCC with a lamellar structure, MPCC exhibits a bulk structure due to the formation of a crosslinking structure. The particle size of MPCC-*x* is less than 2 μm, significantly smaller than that of PCC and MPCC (5–15 μm). The size reduction is attributed to the mechanochemical forces induced by ball-milling, which disrupt the microcrystalline structure and C-C bonds of PC [32,44,45]. HRTEM results (Fig. 3 and Fig. S3) reveal that PCC is a typical soft carbon characterized by a long-range ordered structure, comprising graphite phases and graphite-like phases. The microstructure of MPCC is more disordered with the pseudo-graphite phase. This is primarily attributed to the highly thermally stable crosslinking structure induced by carboxyl groups, which can inhibit the rearrangement of the carbon layers and the development of long-range ordered carbon crystallites. The disruption of the microcrystalline structure induced by ball-milling and the strengthening effect on the carboxylation process further enhance the disorder of the material. As a result, MPCC-*x* exhibit a turbostratic structure of hard carbon with abundant closed pores and distorted carbon layers, accompanied by the disappearance of the graphite phase. The microstructure of carboxyl-induced PC-derived carbon is transformed from graphitic structure to turbostratic structure, facilitating the storage and transport of sodium ions.

The specific surface area and pore size distribution of the obtained carbon were tested using N_2 adsorption-desorption isotherms (Fig. 4a and Fig. S4). All samples exhibit a low specific surface area (<10 $m^2 g^{-1}$), which can effectively prevent the formation of thick SEI layer and improve the ICE. The specific surface area is primarily contributed by mesopores and macropores, facilitating sodium ions transport and electrolyte penetration. The effect of the modification process on the microcrystalline structure of the samples was further analyzed using Raman spectra and X-ray diffraction (XRD). Two characteristic peaks appear in the Raman spectra (Fig. 4b), including defect-induced D-band at ~1350 cm^{-1} and in-plane vibrational G-band of crystalline graphite at ~1580 cm^{-1} [46]. The rations of D-band and G-band area (A_D/A_G) obtained by fitting the Raman spectra (Fig. S5) can be used to describe the structural disorder of materials. The A_D/A_G values increase monotonically from PCC (1.77) to MPCC-2 (3.04), indicating that a combination of surface carboxylation and microstructure disruption leads to a more disordered structure.

The XRD results (Fig. 4c and Fig. S6a) show that the (002) peak for MPCC, MPCC-1 and MPCC-2 is broadened and shifted to a lower angle compared to PCC, indicating a decrease in the graphitization and an enlargement of the interlayer spacing in the materials. To further investigate the microcrystalline state of the obtained carbon, the (002) peaks can be fitted and classified into three types based on the interlayer spacing: graphite (d_{002} < 0.345 nm), graphite-like (0.345 ≤ d_{002} < 0.370 nm) and pseudo-graphitic phase (d_{002} > 0.370 nm) [25,47,48]. In addition, compared with the fit peaks of graphite-like phase, those of pseudo-graphite phase are broader, indicating a gradual reduction in the stacking of graphite layers and a more disordered microstructure (Fig. 4d). The PCC mainly consists of graphite and graphite-like phases. As the surface carboxylation proceeds, the content of the graphite phase gradually decreases and disappears in the MPCC-*x* samples, while the content of graphite-like and pseudo-graphite phases increases, which is consistent with HRTEM results. The structural parameters of obtained carbon are summarized in Tables S4 and S5. The above results show that the microstructure disruption and surface carboxylation treatment successfully transform the PC-based carbon from a long-range ordered structure to a disordered structure with enlarged interlayer spacing.

The reason for the microstructure transformation of the obtained carbon was analyzed by XPS from the perspective of oxygen-containing functional groups (Fig. 4e). The types of functional groups for the obtained carbon show no difference in the O 1s spectra, including C-O, O=C-O and C=O groups. However, the content of functional groups exhibits a notable difference (Fig. S7 and Table S3). Compared with PCC, the content of C-O groups in MPCC, MPCC-1 and MPCC-2 increases significantly, suggesting that the surface carboxylation treatment facilitates the formation of C-O-C bonds during the pyrolysis process. Compared with MPC-1, the C-O content of MPCC-1 is significantly increased, while the proportion of O=C-O is reduced, further demonstrating that the formation of C-O-C originates from the cleavage and reconstruction of O=C-O during pyrolysis [49]. Based on the above results, we propose that the introduced carboxyl groups, acting as an extracyclic unsaturated functional group, are more susceptible to undergoing cleavage-reconstruction or self-crosslinking reactions during pyrolysis. This process leads to the formation of a significant amount of C-O-C linkages, thereby increasing the crosslinking degree of the material. The carbon samples with higher C-O-C content also exhibit a more disordered structure, indicating that the C-O-C groups obtained by carboxyl conversion are key to the microstructure transformation of PC. Such C-O-C groups connecting the adjacent aromatic units act as steric hindrances to inhibit the rearrangement of graphitic microcrystalline fragments, thus resulting in a relatively disordered structure with large interlayer spacing in the PC-derived carbon [28,49]. Conversely, the lower content of C-O-C groups in the PCC sample cannot effectively restrain the graphitization process, resulting in a structure of soft carbon. Compared with PCC, MPCC and MPCC-*x* have higher C=O content, which is beneficial for the adsorption of sodium ions. Additionally, the crosslinking structure with abundant C-O-C groups is conducive to the formation of closed pores. The true density results (Fig. 4f) show a gradual increase in closed pore volume for MPCC and MPCC-1 compared to PCC. The slight decrease in the closed pore volume for MPCC-2 is mainly attributed to the fact that excessive ball-milling results in the formation of smaller microcrystal sizes. The small-sized microcrystals tend to be more densely stacked, resulting in higher true density and lower closed pore volume of MPCC-2 [50]. Since the small interlayer spacing of the graphite phase cannot accommodate the insertion and transport of sodium ions, only accessible closed pores (ACP) surrounded by graphite-like or pseudo-graphite phases can serve as sites for sodium filling [48]. The accessible closed pore volume (ACPV) can be expressed as the closed pore volume multiplied by the content of pseudo-graphite and graphite-like phases, as shown in Fig. S8a. The Small Angle X-ray Scattering (SAXS) results (Fig. S8b) reveal that MPCC-1 exhibits a more pronounced peak at ~0.1 $Å^{-1}$ compared to PCC, which is a typical characteristic of closed pores.

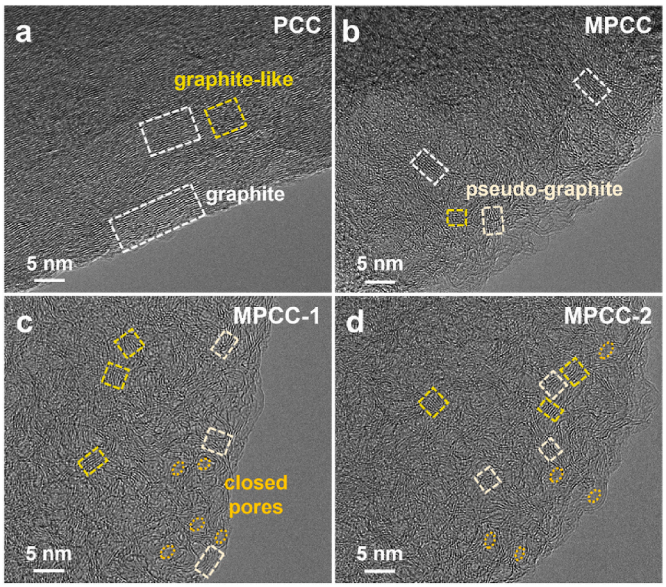

Fig. 3. HRTEM images of (a) PCC, (b) MPCC, (c) MPCC-1 and (d) MPCC-2.

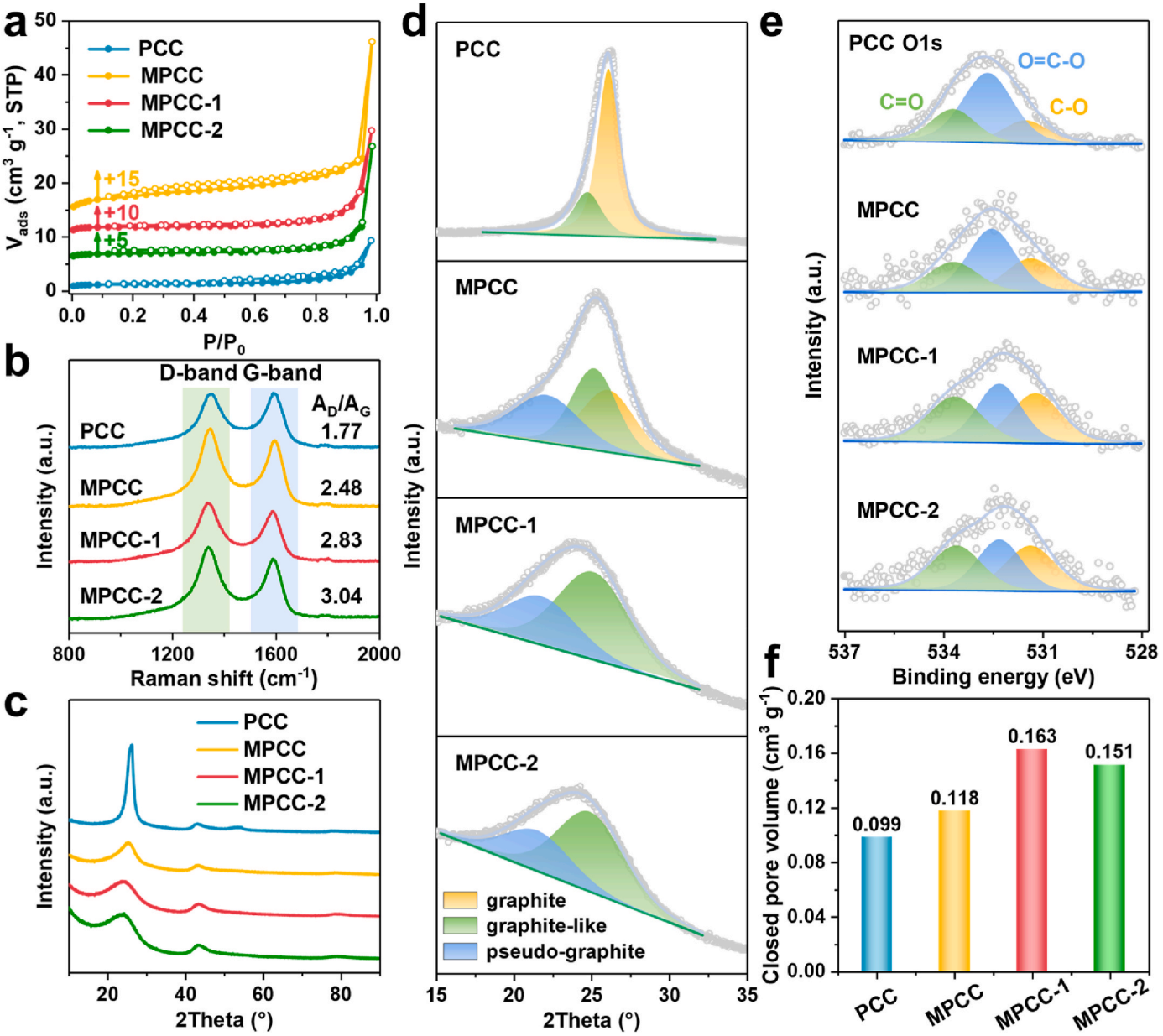

Fig. 4. (a) N_2 adsorption-desorption isotherms, $+x$ represents the number of units by which the isotherm is shifted upward, (b) Raman spectra, (c) XRD patterns, (d) Peak fitting of the (002) peaks, (e) High-resolution O 1s spectra, (f) Closed pore volume of PCC, MPCC, MPCC-1 and MPCC-2.

3.2. Sodium storage properties of petroleum coke-derived carbon

The electrochemical performances of the carbon were evaluated in a half-cell using metallic sodium as the counter electrode. The galvanostatic charge-discharge (GCD) curves of the samples are shown in Fig. 5a. Due to its high graphite phase content and small interlayer spacing, the PCC exhibits a low reversible specific capacity of 106.0 mAh g^{-1}. PCC follows the sodium storage behavior of soft carbon with a prominent sloping region (> 0.1 V) and a negligible plateau region (< 0.1 V). The ICE of PCC is only 62.3 %. Since PCC exhibits a low specific surface area, the capacity loss is mainly attributed to the irreversible insertion behavior of sodium ions in carbon domains with small interlayer spacing rather than the formation of a large amount of SEI [51]. Both MPCC and MPCC-*x* exhibit highly disordered turbostratic structure with large interlayer spacing and abundant accessible closed pores, which facilitate the reversible storage of sodium ions. As a result, MPCC and MPCC-*x* exhibit significantly improved ICE and reversible capacity with high plateau capacity, consistent with hard carbon sodium storage behavior. Among them, MPCC-1 exhibits the highest reversible capacity of 322.0 mAh g^{-1} and ICE of 84.0 %. The slight deterioration of reversible capacity and ICE of MPCC-2 is mainly attributed to excessive ball-milling, which increases defective surfaces and reduces the content of closed pores.

The plateau capacity and sloping capacity of the samples based on the first charge curve are shown in Fig. 5b. The increased reversible capacity of the MPCC and MPCC-*x* is mainly dominated by the plateau capacity, which increases from 28.9 mAh g^{-1} for PCC to 185.8 mAh g^{-1} for MPCC-1. The expansion of interlayer spacing and the increase of accessible closed pores induced by the modification process are crucial for enhancing the plateau capacity of PC-based carbon. The increased sloping capacity benefits from the higher disorder and C=O content. The rate performance results (Fig. 5c) show that the reversible capacity of the samples gradually decreases with the increasing current density. Fig. S9 shows the GCD curves for each sample at different current densities, along with the corresponding plateau capacity and sloping capacity change curves [52]. As shown in Fig. S9f, the reversible capacity

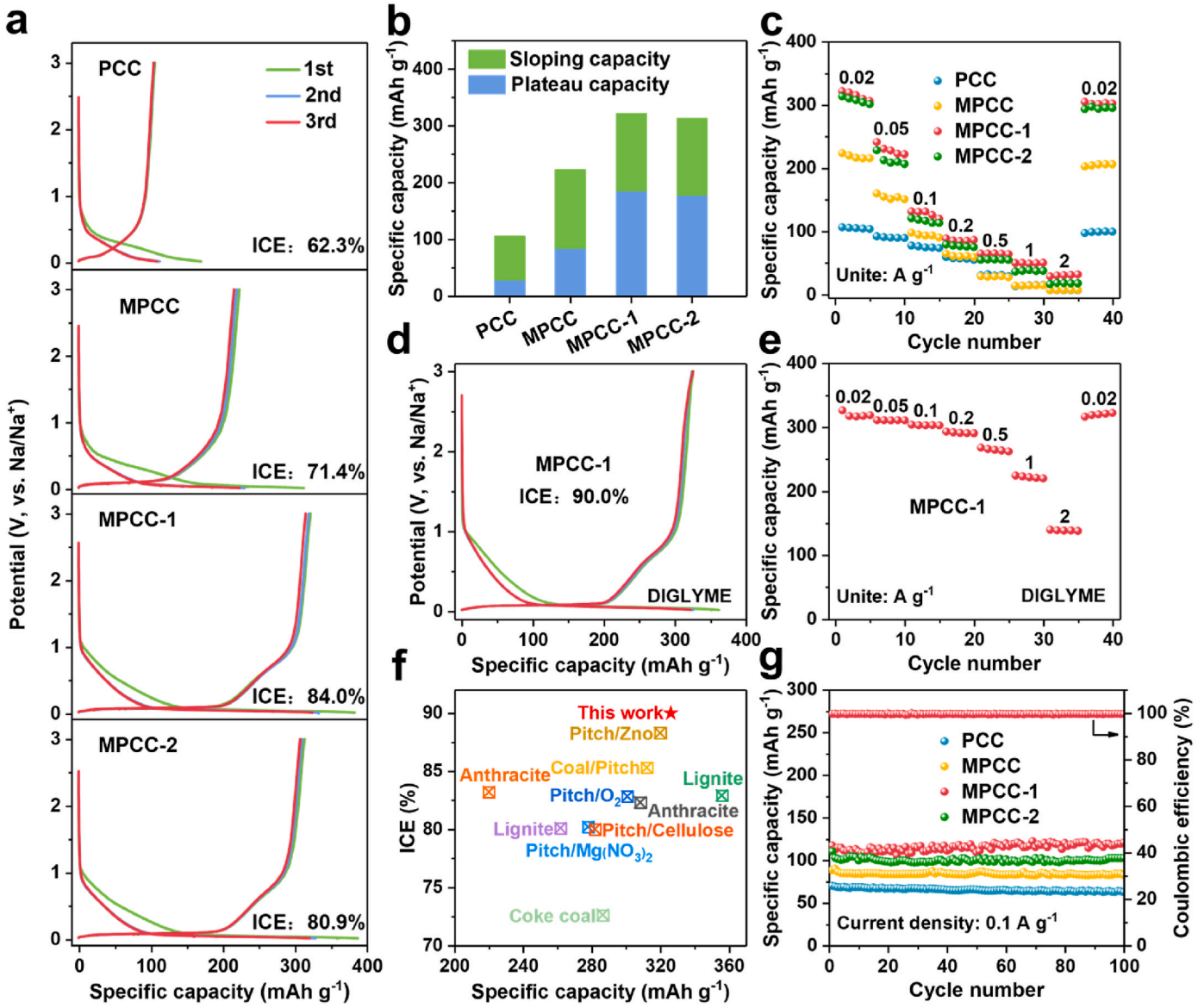

Fig. 5. (a) GCD curves at 20 mA g^{-1}, (b) Capacity contribution of the sloping and plateau region in the first cycle discharge curve, (c) Rate capability of PCC, MPCC, MPCC-1 and MPCC-2. (d) GCD curves at 20 mA g^{-1}, (e) Rate capability of MPCC-1 using ether-based electrolyte. (f) Comparative ICE and specific capacity of soft carbon precursor-derived carbons at low current densities. (g) Cycling performance using ester-based electrolyte at 0.1 A g^{-1}.

decay mainly arises from the rapid loss of plateau capacity, which is related to sluggish dynamics in the plateau region [25]. In addition, the polarization of the metallic sodium electrode in the ester-based electrolyte leads to an earlier response of the cut-off voltage during the half-cell test, which is also an important factor contributing to the rapid decay of plateau capacity [53]. Compared to ester-based electrolytes, the faster de-solvation process and the formation of a thin SEI layer in ether-based electrolytes facilitate faster rate kinetics and provide a more accurate reflection of the rate performance [54]. In the ether-based electrolyte, MPCC-1 exhibits a reversible capacity of 326.3 mAh g^{-1} and an ICE of 90.0 % (Fig. 5d). The decay rate of the plateau and sloping capacity at high current density is significantly reduced, and the reversible capacity of 139.2 mAh g^{-1} is maintained at 2 A g^{-1} (Fig. 5e and Fig. S9g). The above results indicate that the electrolyte plays a decisive role in unlocking the sodium storage potential of materials with a well-designed structure. The reversible capacity and ICE of soft carbon precursor-derived carbon reported recently at low current density are summarized in Fig. 5f and Table S6. MPCC-1 exhibits outstanding reversible capacity and ICE. Additionally, the MPCC-1 exhibits good cycling stability with almost no capacity degradation at 0.1 A g^{-1} after 100 cycles with ester-based electrolyte and 99.5 % capacity retention after 60 cycles with ether-based electrolyte (Fig. 5g, Fig. S9h). After 400 cycles of long-term cycle (Fig. S10), the capacity retention of MPCC-1 is 91.6 %, significantly better than that of PCC (76.5 %).

3.3. *Revealing the sodium storage mechanism of petroleum coke-derived carbon*

The structural changes of MPCC-1 and PCC samples during the first discharge-charge process were studied by in-situ XRD. As shown in Fig. 6a and Fig. S11, the (002) peak of MPCC-1 remains almost unchanged from the open circuit voltage (OCV) to 0.5 V, indicating the sodium adsorption process. When the voltage decreases from 0.5 V to 0.1 V, the (002) peak shifts to a lower angle, indicating the expansion of the interlayer spacing due to the sodium insertion process [55]. Below 0.1 V, the (002) peak exhibits a negligible shift, suggesting that closed pore filling of sodium ions may be occurring. The (002) peak gradually recovers to its original position during the desodiation process,

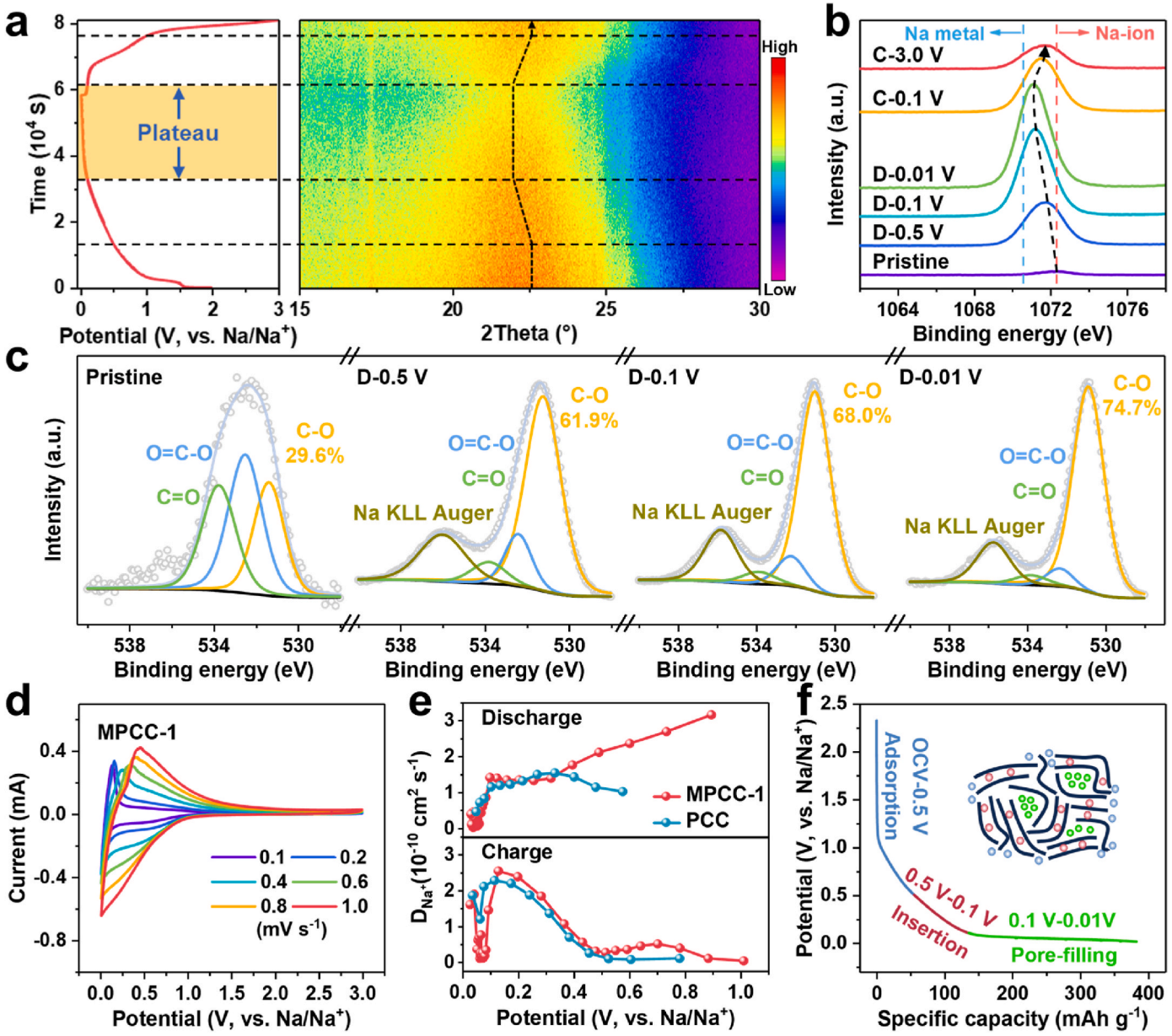

Fig. 6. (a) In-situ XRD patterns, (b) Na 1s at different voltages, (c) O 1s at the stage of pristine and discharge to 0.5 V, 0.1 V, 0.01 V states, (d) CV curves at different scan rates of MPCC-1. (e) Na^+ ions apparent diffusion coefficients of PCC and MPCC-1. (f) Sodiation mechanism for MPCC-1.

suggesting that the large interlayer spacing of MPCC-1 facilitates the reversible sodium storage, consistent with its high ICE. A similar phenomenon is observed for PCC (Fig. S12), except that the position of the graphite peak hardly shifts during the discharge process, suggesting no sodium insertion in graphite domains. During the desodiation process, the (002) peak does not return to its original position, indicating that an irreversible insertion process occurs in the carbon domains with low interlayer spacing. The irreversible insertion process is also the main reason for its low ICE. The in-situ XRD analysis of the above two samples shows that the sloping capacity of PC-derived carbon stems from both the sodium adsorption and insertion processes, while plateau capacity may be derived from the closed pore filling process. Furthermore, the presence of graphite domains does not effectively store and transport sodium ions and therefore should be minimized in the material preparation process.

The chemical bonding states of sodium in MPCC-1 during the first discharge-charge process were investigated by ex-situ XPS after removing SEI by argon ion sputtering. As shown in Fig. 6b, the Na 1s peak on the pristine electrode is weak and broad, attributed to the sodium carboxymethyl cellulose binder. As the sodiation process proceeds, the intensity of the Na 1s peak increases and shifts towards the binding energy of metallic sodium, indicating the insertion of sodium into the carbon layers [56]. When discharged to 0.1 V, the peak intensity increases significantly, indicating that sodium is beginning to fill the closed pores. During the desodiation process, the intensity of the Na 1s peak decreases and gradually shifts toward the binding energy of Na-ions, indicating the reversibility of the closed pore filling process. The ex-situ XPS Na 1s spectra before sputtering in Fig. S13e show no shift in the peak position for Na 1s across different voltage states (discharged to 0.01 V and charged to 3.0 V), suggesting that the signal of Na 1s after sputtering comes from Na stored in carbon matrix rather than SEI. The deconvolution of O 1s spectra of different sodiation states was used to study the interaction between Na-ions and oxygen-containing functional groups (Fig. 6c and Table S7). The C=O content decreases gradually accompanied by a sharp increase in the C-O content during the discharge process. The opposite variation can be found during the

charge process (Fig. S14), indicating a reversible transformation of C=O to C-O bonds. The functional group content changes sharply above 0.5 V, while a slower variation can be observed below 0.5 V. This phenomenon confirms that the redox reaction between C=O and Na-ions occurs primarily above 0.5 V, which is consistent with the in-situ XRD results.

The reaction kinetics of MPCC-1 and PCC were analyzed by cyclic voltammetry (CV) and galvanostatic intermittent titration technique (GITT) to further determine the sodium storage mechanism. As shown in Fig. S15, a pair of redox peaks at the voltage region of 0.10–0.01 V in the CV curves of MPCC-1 and PCC correspond to the plateau region in the GCD curves. The redox peak of MPCC-1 is more pronounced compared to PCC, corresponding to its higher plateau capacity. MPCC-1 exhibits small irreversible peaks in both ester- and ether-based electrolytes, indicating minimal electrolyte decomposition during cycling, which contributes to the high ICE. Furthermore, the power-law relationship ($i = av^b$) between scan rate (v) and peak current (i) was utilized to calculate the b value, analyzing the sodium storage behavior of the plateau region (Fig. 6d and Fig. S16) [57]. The b values of MPCC-1 and PCC in the plateau region are 0.67 and 0.55, reflecting a diffusion-controlled process. The higher b value indicates that MPCC-1 has faster reaction kinetics than PCC [22]. To quantitatively analyze the contribution of capacitive-controlled and diffusion-controlled processes, the CV curves of the electrodes are analyzed using the equation $i(V) = k_1v + k_2v^{1/2}$, as shown in Fig. S16c and S16d. At a scan rate of 0.1 mV s^{-1}, the capacitive contribution ratio for MPCC-1 is 39.5 %. As the scan rate increases, the capacitive contribution ratio rises to 85.2 %. A similar trend is observed for PCC. At each corresponding scan rate, the capacitive contribution ratio of MPCC-1 is consistently higher than that of PCC, which further illustrates the faster sodium storage kinetics of MPCC-1. The Na^+ diffusion coefficient (D^+_{Na}) of the two electrodes were calculated by GITT analysis, as shown in Fig. 6e and Fig. S17. The D^+_{Na} values maintain a high value during the initial sodiation stage, corresponding to the sodium adsorption on surface active sites. As the sodiation process proceeds, the D^+_{Na} values gradually decrease and then drop rapidly at 0.1 V. Based on the in-situ XRD results, this stage corresponds to the sodium insertion process. Below 0.1 V, the D^+_{Na} values of PCC continue to decrease, indicating unchanged sodium insertion behavior, whereas the D^+_{Na} values of MPCC-1 show a U-turn feature, which can be attributed to the closed pore filling of sodium ions [10,58]. MPCC-1 exhibits higher D^+_{Na} values than PCC. Overall, the regulation of the carbon microcrystalline structure induced by the surface carboxylation process facilitates fast reaction kinetics for sodium transport and storage in the MPCC-1 anode.

The relationship between accessible closed pore volume and plateau capacity is shown in Fig. S18, which can be described by equation $Y = 1149 * X$ with a correlation coefficient of 0.99. The slope is similar to the theoretical specific capacity of metallic sodium (1128 mAh cm^{-3}), which further confirms that the plateau capacity is derived from the accessible closed pore filling process. Based on the above analysis, the sodium storage process of the PC-based carbon anode can be divided into three stages (Fig. 6f): (1) The high-voltage sloping region (OCV-0.5 V) corresponds to the adsorption of Na^+ on surface sites, including edges, defects, and C=O groups. (2) The low-voltage sloping region (0.5 V–0.1 V) corresponds to the process of Na^+ insertion in the non-graphite phase. (3) The plateau region (0.1 V–0.01 V) corresponds to the process of Na^+ filling in accessible closed pores. The adsorption/insertion-filling mechanism is validated as a reasonable sodium storage model for PC-based carbon anodes.

3.4. Assembling full cell using petroleum coke-derived carbon as the anode material

To evaluate the potential of MPCC-1 for practical applications, a full cell was assembled by matching it with an O3-$Na_{0.9}TMO_2$ cathode (Fig. 7a). The GCD curve of O3-$Na_{0.9}TMO_2$ is shown in Fig. S19a. To achieve a good charge balance, the capacity ratio of the negative to

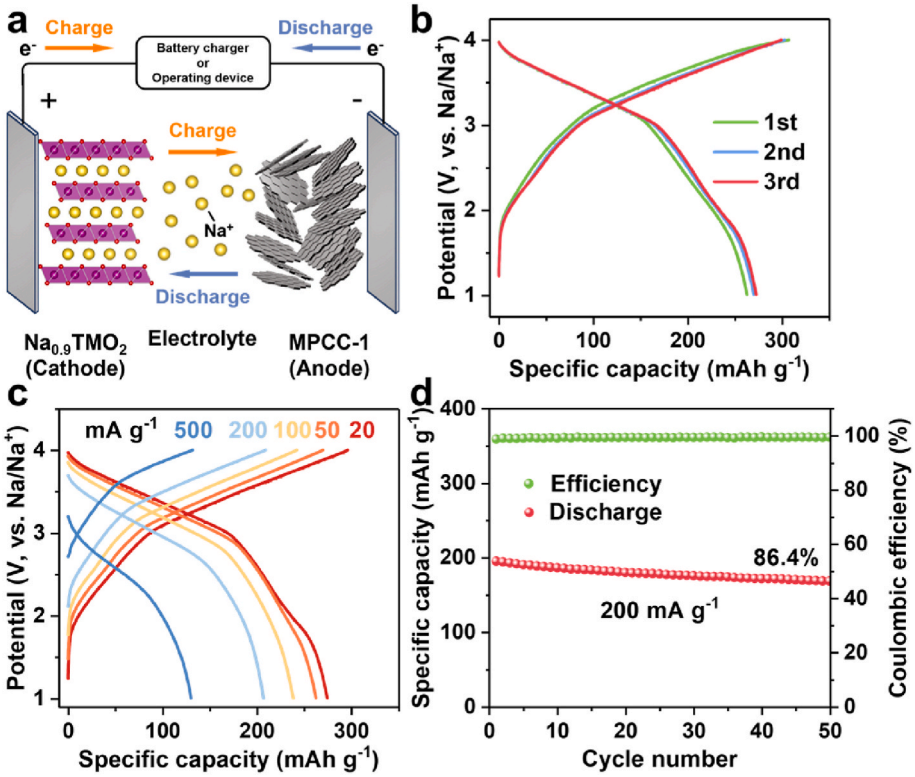

Fig. 7. (a) Schematic illustration of MPCC-1//$Na_{0.9}TMO_2$ SIB. (b) Initial three charge-discharge curves of MPCC-1//$Na_{0.9}TMO_2$ SIB at the current density of 20 mA g^{-1}. (c) Charge-discharge curves of MPCC-1//$Na_{0.9}TMO_2$ SIB at various current densities. (d) Cycling performance of MPCC-1//$Na_{0.9}TMO_2$ SIB at the current density of 200 mA g^{-1}.

positive electrodes (N/P ratio) is kept in the range of 1–1.05. The MPCC-1//$Na_{0.9}TMO_2$ sodium-ion battery exhibits a reversible specific capacity of 273.2 mAh g^{-1} at 20 mA g^{-1} (based on the active material mass of the anode) with an average operating voltage of 3.17 V (Fig. 7b). As shown in Fig. 7c, when the current density is increased to 500 mA g^{-1}, the full cell still exhibits a high capacity of 130.4 mAh g^{-1}, demonstrating excellent rate performance. In addition, the full cell exhibits excellent cycling stability with a capacity retention of 86.4 % after 50 cycles at 200 mA g^{-1} (Fig. 7d). Based on the total mass of the anode and cathode active materials, the energy density of the MPCC-1//$Na_{0.9}TMO_2$ is 228.1 Wh kg^{-1}, which is competitive among soft carbon precursor-derived materials (Table S8). In addition, the MPCC-1//$Na_{0.9}TMO_2$ SIB exhibits a reversible specific capacity of 317.9 mAh g^{-1} using ether-based electrolyte at 20 mA g^{-1}. The full cell operates with an average voltage of 3.06 V, resulting in an energy density of 253.3 Wh kg^{-1} (Fig. S19b). This indicates that MPCC-1 has a good prospect for practical application in SIBs.

4. Conclusion

In summary, a carboxyl-induced microcrystalline structure regulation strategy has been developed to inhibit the graphitization of petroleum coke-based carbon, achieving the transformation from long-range ordered soft carbon to disordered turbostratic structure-dominated hard carbon. The Diels-Alder reaction between maleic anhydride and the graphitic edges of ball-milled PC introduces abundant carboxyl groups in the PC precursor, which are then converted into C-O-C groups to bridge adjacent aromatic fragments during pyrolysis. The formation of C-O-C groups acts as steric hindrances to prevent the aggregation of graphitic microcrystalline fragments, thereby retarding graphitization and leading to the formation of PC-based hard carbon with large interlayer spacing and abundant closed pores. The optimized MPCC-1 exhibits a high reversible capacity of 326.3 mAh g^{-1}, a high ICE of 90.0 %, and excellent cycling stability with 91.6 % retention after 400 cycles. The fabricated MPCC-1//$Na_{0.9}TMO_2$ full cell exhibits a high energy density of 228.1 Wh kg^{-1}. This work introduces an innovative approach to regulate the microcrystalline structure and establishes a solid foundation for the commercial application of soft carbon precursors in anode materials for SIBs.

CRediT authorship contribution statement

Jia-He Lv: Writing – review & editing, Writing – original draft, Investigation, Formal analysis, Data curation, Conceptualization. **Bin He:** Writing – review & editing. **Lin-Tao Lv:** Investigation, Formal analysis. **Ming-Kang Yan:** Writing – review & editing, Investigation. **Jun-Chen Zhong:** Writing – review & editing, Investigation. **Guang-Ping Hao:** Supervision, Project administration. **Wen-Cui Li:** Writing – review & editing, Supervision, Project administration, Funding acquisition, Conceptualization.

Declaration of competing interest

The authors declare that they have no known competing financial interests or personal relationships that could have appeared to influence the work reported in this paper.

Acknowledgements

This work was financially supported by the National Natural Science Foundation of China (Nos. 22478066 and 22075038).

Appendix A. Supplementary data

Supplementary data to this article can be found online at https://doi.org/10.1016/j.jpowsour.2025.236505.

Data availability

Data will be made available on request.

References

[1] J. Lu, Z. Zhang, Y. Zheng, Y. Gao, In situ transmission electron microscopy for sodium-ion batteries, Adv. Mater. 35 (2023) 2300359, https://doi.org/10.1002/adma.202300359.
[2] J.L. Xia, D. Yan, L.P. Guo, X.L. Dong, W.C. Li, A.H. Lu, Hard carbon nanosheets with uniform ultramicropores and accessible functional groups showing high realistic capacity and superior rate performance for sodium-ion storage, Adv. Mater. 32 (2020) 2000447, https://doi.org/10.1002/adma.202000447.
[3] H. Ma, M. Jiang, Z. Hou, T. Li, X. Zhang, Y. Gao, J. Peng, Y. Li, J.G. Wang, Medium-mediated high-crystalline prussian blue toward exceptionally boosted sodium energy storage, Energy Storage Mater. 70 (2024) 103411, https://doi.org/10.1016/j.ensm.2024.103411.
[4] R. Usiskin, Y. Lu, J. Popovic, M. Law, P. Balaya, Y. Hu, J. Maier, Fundamentals, status and promise of sodium-based batteries, Nat. Rev. Mater. 6 (2021) 1020–1035, https://doi.org/10.1038/s41578-021-00324-w.
[5] D. Kim, O.L. Li, J. Kang, Maximizing the rate capability of carbon-based anode materials for sodium-ion batteries, J. Power Sources 481 (2021) 228973, https://doi.org/10.1016/j.jpowsour.2020.228973.
[6] V. Palomares, M. Casas-Cabanas, E. Castillo-Martnez, M.H. Han, T. Rojo, Update on Na-based battery materials. A growing research path, Energy Environ. Sci. 6 (2013) 2312–2337, https://doi.org/10.1039/c3ee41031e.
[7] X. Chen, J. Tian, P. Li, Y. Fang, Y. Fang, X. Liang, J. Feng, J. Dong, X. Ai, H. Yang, Y. Cao, An overall understanding of sodium storage behaviors in hard carbons by an "adsorption-intercalation/filling" hybrid mechanism, Adv. Energy Mater. 12 (2022) 2200886, https://doi.org/10.1002/aenm.202200886.
[8] D. Alvira, D. Antorán, J.J. Manyà, Plant-derived hard carbon as anode for sodium-ion batteries: a comprehensive review to guide interdisciplinary research, Chem. Eng. J. 447 (2022) 137468, https://doi.org/10.1016/j.cej.2022.137468.
[9] M. Jiang, N. Sun, R. Ali Soomro, B. Xu, The recent progress of pitch-based carbon anodes in sodium-ion batteries, J. Energy Chem. 55 (2021) 34–47, https://doi.org/10.1016/j.jechem.2020.07.002.
[10] K. Wang, F. Sun, H. Wang, D. Wu, Y. Chao, J. Gao, G. Zhao, Altering thermal transformation pathway to create closed pores in coal-derived hard carbon and boosting of Na^+ plateau storage for high-performance sodium-ion battery and sodium-ion capacitor, Adv. Funct. Mater. 32 (2022) 2203725, https://doi.org/10.1002/adfm.202203725.
[11] Y. Zhao, Z. Hu, W. Zhou, P. Gao, Z. Liu, J. Liu, C. Fan, J. Liu, Advanced structural engineering design for tailored microporous structure via adjustable graphite sheet angle to enhance sodium-ion storage in anthracite-based carbon anode, Adv. Funct. Mater. 34 (2024) 2405174, https://doi.org/10.1002/adfm.202405174.
[12] P. Zheng, W. Zhou, Y. Mo, B. Zheng, M. Han, Q. Zhong, W. Yang, P. Gao, L. Yang, J. Liu, Multi boron-doping effects in hard carbon toward enhanced sodium ion storage, J. Energy Chem. 100 (2025) 730–738, https://doi.org/10.1016/j.jechem.2024.09.024.
[13] L. Ren, W. Hua, Z. Hou, J.G. Wang, Rational construction of CoP@C hollow structure for ultrafast and stable sodium energy storage, Rare Met. 41 (2022) 1859–1869, https://doi.org/10.1007/s12598-021-01930-x.
[14] H. Zhang, L. Luo, M. Guo, D. Zhang, Z. Huang, X. Wang, F. Gao, X. Chen, M. Terrones, Y. Wang, Biomimetic mineralization coupling with seeds-induced foaming for optimizing carbon microstructure towards ultrafast sodium ion storage, J. Power Sources 613 (2024) 234875, https://doi.org/10.1016/j.jpowsour.2024.234875.
[15] H. Zhang, D. Zhang, M. Guo, Z. Huang, X. Wang, C. Gao, F. Gao, M. Terrones, Y. Wang, Combustion activation induced solid-state synthesis for N, B co-doped carbon/zinc borate anode with a boosting of sodium storage performance, Adv. Sci. 10 (2023) 2207751, https://doi.org/10.1002/advs.202207751.
[16] H. Zhang, G. Huang, L. Luo, D. Zhang, F. Gao, C. Gao, X. Wang, X. Chen, M. Terrones, Y. Wang, Biomimetic-mineralization-assisted self-activation creates a delicate porous structure in carbon material for high-rate sodium storage, ACS Appl. Mater. Interfaces 16 (2024) 23374–23386, https://doi.org/10.1021/acsami.4c03425.
[17] H. Zhang, F. Gao, D. Zhang, C. Gao, G. Huang, Z. Zhang, Y. Liu, M. Terrones, J. Wei, Y. Wang, Biomimetic mineralization synergistic combustion activation to construct honeycomb porous carbon anode for sodium-ion batteries, Carbon 230 (2024) 119602, https://doi.org/10.1016/j.carbon.2024.119602.
[18] P. Wang, Y.J. Guo, W.P. Chen, H. Duan, H. Ye, H.R. Yao, Y.X. Yin, F.F. Cao, Self-supported hard carbon anode from fungus-treated basswood towards sodium-ion batteries, Nano Res. 16 (2023) 3832–3838, https://doi.org/10.1007/s12274-022-4708-5.
[19] P. Wang, G. Zhang, X.Y. Wei, R. Liu, J.J. Gu, F.F. Cao, Bioselective synthesis of a porous carbon collector for high-performance sodium-metal anodes, J. Am. Chem. Soc. 143 (2021) 3280–3283, https://doi.org/10.1021/jacs.0c12098.
[20] J. Zhao, X.X. He, W.H. Lai, Z. Yang, X.H. Liu, L. Li, Y. Qiao, Y. Xiao, L. Li, X. Wu, S. L. Chou, Catalytic defect-repairing using manganese ions for hard carbon anode with high-capacity and high-initial-coulombic-efficiency in sodium-ion batteries, Adv. Energy Mater. 13 (2023) 2300444, https://doi.org/10.1002/aenm.202300444.
[21] C. Fan, R. Zhang, X. Luo, Z. Hu, W. Zhou, W. Zhang, J. Liu, J. Liu, Epoxy phenol novolac resin: a novel precursor to construct high performance hard carbon anode

toward enhanced sodium-ion batteries, Carbon 205 (2023) 353–364, https://doi.org/10.1016/j.carbon.2023.01.048.
[22] Z. Zheng, S. Hu, W. Yin, J. Peng, R. Wang, J. Jin, B. He, Y. Gong, H. Wang, H.J. Fan, CO_2-etching creates abundant closed pores in hard carbon for high-plateau-capacity sodium storage, Adv. Energy Mater. 14 (2024) 2303064, https://doi.org/10.1002/aenm.202303064.
[23] G. Zhang, L. Zhang, Q. Ren, L. Yan, F. Zhang, W. Lv, Z. Shi, Tailoring a phenolic resin precursor by facile pre-oxidation tactics to realize a high-initial-coulombic-efficiency hard carbon anode for sodium-ion batteries, ACS Appl. Mater. Interfaces 13 (2021) 31650–31659, https://doi.org/10.1021/acsami.1c06168.
[24] L. Yan, J. Wang, Q. Ren, L. Fan, B. Liu, L. Zhang, L. He, X. Mei, Z. Shi, In-situ graphene-coated carbon microsphere as high initial coulombic efficiency anode for superior Na/K-ion full cell, Chem. Eng. J. 432 (2022) 133257, https://doi.org/10.1016/j.cej.2021.133257.
[25] M. Song, Z. Yi, R. Xu, J. Chen, J. Cheng, Z. Wang, Q. Liu, Q. Guo, L. Xie, C. Chen, Towards enhanced sodium storage of hard carbon anodes: regulating the oxygen content in precursor by low-temperature hydrogen reduction, Energy Storage Mater. 51 (2022) 620–629, https://doi.org/10.1016/j.ensm.2022.07.005.
[26] M. Zhang, Y. Li, F. Wu, Y. Bai, C. Wu, Boost sodium-ion batteries to commercialization: strategies to enhance initial coulombic efficiency of hard carbon anode, Nano Energy 82 (2021) 105738, https://doi.org/10.1016/j.nanoen.2020.105738.
[27] H. Chen, N. Sun, Q. Zhu, R.A. Soomro, B. Xu, Microcrystalline hybridization enhanced coal-based carbon anode for advanced sodium-ion batteries, Adv. Sci. 9 (2022) 2200023, https://doi.org/10.1002/advs.202200023.
[28] Y. Shao, Q. Yang, Y. Zhang, N. Jiang, Y. Hao, K. Qu, Y. Du, J. Qi, Y. Li, Y. Tang, X. Lu, L. Zhang, J. Qiu, A universal method for regulating carbon microcrystalline structure for high-capacity sodium storage: binding energy as descriptor, ACS Nano 17 (2023) 24012–24021, https://doi.org/10.1021/acsnano.3c08889.
[29] H. He, J. He, H. Yu, L. Zeng, D. Luo, C. Zhang, Dual-interfering chemistry for soft-hard carbon translation toward fast and durable sodium storage, Adv. Energy Mater. 13 (2023) 2300357, https://doi.org/10.1002/aenm.202300357.
[30] R. Alcántara, J.M. Jimenez Mateos, J.L. Tirado, Negative electrodes for lithium- and sodium-ion batteries obtained by heat-treatment of petroleum cokes below 1000°C, J. Electrochem. Soc. 149 (2002) A201–A205, https://doi.org/10.1149/1.1431963.
[31] F. Sun, H. Wang, Z. Qu, K. Wang, L. Wang, J. Gao, J. Gao, S. Liu, Y. Lu, Carboxyl-dominant oxygen rich carbon for improved sodium ion storage: synergistic enhancement of adsorption and intercalation mechanisms, Adv. Energy Mater. 11 (2021) 2002981, https://doi.org/10.1002/aenm.202002981.
[32] J. Zhang, Y. Lei, L. Zhou, X. Chen, S. Huang, L. Liu, H. Liu, S. Dou, J. Xu, Ball-milling synthesis of richly oxygenated graphene-like nanoplatelets from used lithium ion batteries and its application for high performance sodium ion battery anode, Adv. Funct. Mater. (2024) 2314160, https://doi.org/10.1002/adfm.202314160.
[33] S.C. Lee, Y.H. Kim, J.H. Park, D. Susanto, J.Y. Kim, J. Han, S.C. Jun, K.Y. Chung, Mechanical activation of graphite for Na-ion battery anodes: unexpected reversible reaction on solid electrolyte interphase via x-ray analysis, Adv. Sci. (2024) 2401022, https://doi.org/10.1002/advs.202401022.
[34] H. Chen, N. Sun, Y. Wang, R.A. Soomro, B. Xu, One stone two birds: pitch assisted microcrystalline regulation and defect engineering in coal-based carbon anodes for sodium-ion batteries, Energy Storage Mater. 56 (2023) 532–541, https://doi.org/10.1016/j.ensm.2023.01.042.
[35] X. Yin, Y. Zhao, X. Wang, X. Feng, Z. Lu, Y. Li, H. Long, J. Wang, J. Ning, J. Zhang, Modulating the graphitic domains of hard carbons derived from mixed pitch and resin to achieve high rate and stable sodium storage, Small 18 (2022) 2105568, https://doi.org/10.1002/smll.202105568.
[36] J. Seo, I. Jeon, J. Baek, Mechanochemically driven solid-state Diels-Alder reaction of graphite into graphene nanoplatelets, Chem. Sci. 4 (2013) 4273–4277, https://doi.org/10.1039/c3sc51546j.
[37] J. Seo, J. Baek, A solvent-free Diels-Alder reaction of graphite into functionalized graphene nanosheets, Chem. Commun. 50 (2014) 14651–14653, https://doi.org/10.1039/C4CC07173E.
[38] M. Kang, H. Zhao, J. Ye, W. Song, H. Shen, J. Mi, Z. Li, Adsorption dominant sodium storage in three-dimensional coal-based graphite microcrystal/graphene composites, J. Mater. Chem. A 7 (2019) 7565–7572, https://doi.org/10.1039/C8TA12062E.
[39] X. Liu, J. Wang, T. Liao, Y. Li, X. Fan, F. Zhang, W. Peng, Electron transfer route tuning caused by photo-irradiation: stability enhancement of n-doped carbon materials in Fenton-like reactions, Appl. Catal. B Environ. 340 (2024) 123261, https://doi.org/10.1016/j.apcatb.2023.123261.
[40] D. Luo, J. Xu, Q. Guo, L. Fang, X. Zhu, Q. Xia, H. Xia, Surface-dominated sodium storage towards high capacity and ultrastable anode material for sodium-ion batteries, Adv. Funct. Mater. 28 (2018) 1805371, https://doi.org/10.1002/adfm.201805371.
[41] A. Ma, S. Zhao, H. Luo, Z. Sun, X. Xie, Y. Liao, X. Liang, H. Li, Mercury removal from coal-fired flue gas of high-sulfur petroleum coke activated by pyrolysis and mechanochemical method, Chem. Eng. J. 429 (2022) 132154, https://doi.org/10.1016/j.cej.2021.132154.
[42] Y. Zhao, H. Hu, L. Jin, X. He, B. Wu, Pyrolysis behavior of vitrinite and inertinite from Chinese Pingshuo coal by TG-MS and in a fixed bed reactor, Fuel Process. Technol. 92 (2011) 780–786, https://doi.org/10.1016/j.fuproc.2010.09.005.
[43] X. Yu, D. Yu, G. Yu, F. Liu, J. Han, J. Wu, M. Xu, Temperature-resolved evolution and speciation of sulfur during pyrolysis of a high-sulfur petroleum coke, Fuel 295 (2021) 120609, https://doi.org/10.1016/j.fuel.2021.120609.
[44] I. Jeon, H. Choi, S. Jung, J. Seo, M. Kim, L. Dai, J. Baek, Large-scale production of edge-selectively functionalized graphene nanoplatelets via ball milling and their use as metal-free electrocatalysts for oxygen reduction reaction, J. Am. Chem. Soc. 135 (2013) 1386–1393, https://doi.org/10.1021/ja3091643.
[45] I. Jeon, Y. Shin, G. Sohn, H. Choi, S. Bae, J. Mahmood, S. Jung, J. Seo, M. Kim, D. Wook Chang, L. Dai, J. Baek, Edge-carboxylated graphene nanosheets via ball milling, Proc. Natl. Acad. Sci. USA 109 (2012) 5588–5593, https://doi.org/10.1073/pnas.1116897109.
[46] J.L. Xia, A.H. Lu, X.F. Yu, W.C. Li, Rational design of a trifunctional binder for hard carbon anodes showing high initial coulombic efficiency and superior rate capability for sodium-ion batteries, Adv. Funct. Mater. 31 (2021) 2104137, https://doi.org/10.1002/adfm.202104137.
[47] Y. Zeng, J. Yang, H. Yang, Y. Yang, J. Zhao, Bridging microstructure and sodium-ion storage mechanism in hard carbon for sodium ion batteries, ACS Energy Lett. 9 (2024) 1184–1191, https://doi.org/10.1021/acsenergylett.3c02751.
[48] J.H. Lv, J.S. Wang, B. He, T. Wu, A.H. Lu, W. Zhang, J. Xu, W. Yin, G.P. Hao, W. C. Li, Revealing an extended adsorption/insertion-filling sodium storage mechanism in petroleum coke-derived amorphous carbon, Adv. Sci. (2024) 2407538, https://doi.org/10.1002/advs.202407538.
[49] X. Tang, F. Xie, Y. Lu, Z. Chen, X. Li, H. Li, X. Huang, L. Chen, Y. Pan, Y. Hu, Intrinsic effects of precursor functional groups on the Na storage performance in carbon anodes, Nano Res. 16 (2023) 12579–12586, https://doi.org/10.1007/s12274-023-5643-9.
[50] Y. Wang, Z. Yi, L. Xie, Y. Mao, W. Ji, Z. Liu, X. Wei, F. Su, C.M. Chen, Releasing free radicals in precursor triggers the formation of closed pores in hard carbon for sodium-ion batteries, Adv. Mater. (2024) 2401249, https://doi.org/10.1002/adma.202401249.
[51] Z. Jian, C. Bommier, L. Luo, Z. Li, W. Wang, C. Wang, P.A. Greaney, X. Ji, Insights on the mechanism of Na-ion storage in soft carbon anode, Chem. Mater. 29 (2017) 2314–2320, https://doi.org/10.1021/acs.chemmater.6b05474.
[52] B. Zheng, W. Zhou, H. Liu, S. Chen, P. Gao, Z. Wang, J. Liu, Surface chemistry induced robust SEI on graphite surface via soft carbon coating enables fast lithium storage, Carbon 218 (2024) 118729, https://doi.org/10.1016/j.carbon.2023.118729.
[53] Z. Tang, D. Jiang, Z. Fu, J. Zhou, R. Liu, R. Zhang, D. Sun, A.S. Dhmees, Y. Tang, H. Wang, Regulating pseudo-graphitic domain and closed pores to facilitate plateau sodium storage capacity and kinetics for hard carbon, Small Methods (2024) 2400509, https://doi.org/10.1002/smtd.202400509.
[54] X. Yi, X. Li, J. Zhong, S. Wang, Z. Wang, H. Guo, J. Wang, G. Yan, Unraveling the mechanism of different kinetics performance between ether and carbonate ester electrolytes in hard carbon electrode, Adv. Funct. Mater. 32 (2022) 2209523, https://doi.org/10.1002/adfm.202209523.
[55] J.C. Hyun, H.M. Jin, J.H. Kwak, S. Ha, D.H. Kang, H.S. Kim, S. Kim, M. Park, C. Y. Kim, J. Yoon, J.S. Park, J. Kim, H. Lim, S.Y. Cho, H. Jin, Y.S. Yun, Design guidelines for a high-performance hard carbon anode in sodium ion batteries, Energy Environ. Sci. 17 (2024) 2856–2863, https://doi.org/10.1039/D4EE00315B.
[56] X. Yin, Z. Lu, J. Wang, X. Feng, S. Roy, X. Liu, Y. Yang, Y. Zhao, J. Zhang, Enabling fast Na^+ transfer kinetics in the whole-voltage-region of hard-carbon anodes for ultrahigh-rate sodium storage, Adv. Mater. 34 (2022) 2109282, https://doi.org/10.1002/adma.202109282.
[57] Q. Ren, J. Wang, L. Yan, W. Lv, F. Zhang, L. Zhang, B. Liu, Z. Shi, Manipulating free-standing, flexible and scalable microfiber carbon papers unlocking ultra-high initial coulombic efficiency and storage sodium behavior, Chem. Eng. J. 425 (2021) 131656, https://doi.org/10.1016/j.cej.2021.131656.
[58] J. Yang, X. Wang, W. Dai, X. Lian, X. Cui, W. Zhang, K. Zhang, M. Lin, R. Zou, K. P. Loh, Q.H. Yang, W. Chen, From micropores to ultra-micropores inside hard carbon: toward enhanced capacity in room-/low-temperature sodium-ion storage, Nano-Micro Lett. 13 (2021) 98, https://doi.org/10.1007/s40820-020-00587-y.